Optimal Design of Permeable Fiber Network Structures for Fog Harvesting

Optimal Design of Permeable Fiber Network Structures for Fog Harvesting

Kyoo-Chul Park[1‡], Shreerang S. Chhatre[2†‡], Siddarth Srinivasan[2],

Robert E. Cohen[2], Gareth H. McKinley[1*]*

[1] Department of Mechanical Engineering, Massachusetts Institute of Technology, Cambridge, MA 02139, USA

[2] Department of Chemical Engineering, Massachusetts Institute of Technology, Cambridge, MA 02139, USA

KEYWORDS

fog collection, woven mesh, fluid mechanics, surface wettability, droplet deposition

ABSTRACT

Fog represents a large, untapped source of potable water, especially in arid climates. Numerous plants and animals use textural as well as chemical features on their surfaces to harvest this precious resource. In this work, we investigate the influence of surface wettability characteristics, length scale, and weave density on the fog harvesting capability of woven meshes. We develop a combined hydrodynamic and surface wettability model to predict the overall fog collection efficiency of the meshes and cast the findings in the form of a design chart. Two limiting surface wettability constraints govern re-entrainment of collected droplets and clogging of mesh openings. Appropriate tuning of the wetting characteristics of the surfaces, reducing the wire radii, and optimizing the wire spacing all lead to more efficient fog collection. We use a family of coated meshes with a directed stream of fog droplets to simulate a natural foggy environment and demonstrate a five-fold enhancement in the fog-collecting efficiency of a conventional polyolefin mesh. The design rules developed in this work can be applied to select a mesh surface with optimal topography and wetting characteristics to harvest enhanced water fluxes over a wide range of natural convected fog environments.

Introduction

According to a recent UN water crisis report by the Food and Agriculture Organization[1] "fog collection technology appears to be an extremely promising and low-cost water harvesting system for drinking water, crop irrigation, livestock beverage and forest restoration in dryland mountains." The UN authors go on to note that the growing global water crisis is a major issue threatening more than 2 billion people in arid regions. To recognize the significance of the water crisis, the UN declared the period 2005-2015 as International Decade for Action "Water for Life" and UNESCO recently launched the International Year for Water Cooperation 2013. As one part of the solution to the water crisis, fog harvesting has already been successfully demonstrated in the field in more than 17 countries over recent decades. [2-8]

The fog harvesting capability of plants and animals have been studied extensively (Figure 1a, 1b).[9-17] The Namib desert beetle (*Stenocara gracilipes*) survives by drinking fog water that it collects on its wing case.[10, 15] A grass (*Stipagrostis sabulicola*) in the same region employs an anisotropic microstructure on its thin long leaves to direct water droplets towards its roots.[16] Tree canopies with slender leaves (*Pinus radiata* and *Casuarina equisetifolia*) also harvest water from fog (Figure 1a).[11-13] Sticky spider webs[17] decorated with tiny water droplets collected from morning fog are a common sight (Figure 1b).[18]

Inspired by such natural phenomena, researchers have constructed fog harvesting meshes,[3-7] which can be characterized by the fiber radius R and the half spacing D of the mesh (Figure 1c-e). The goal is to maximize the efficiency (denoted by η) at which the liquid water content is extracted from the incident moist air stream. Solid structures placed in a wind stream (with unperturbed velocity v_0) deflect the air, but the fog droplets (of radius r_{fog}), have a tendency to

migrate across streamlines due to their higher inertia and impact the solid fibers. This migration is controlled by the Stokes number, $St = t_{particle}/t_{flow} = \left(2\rho_{water} r_{fog}^2/9\mu_{air}\right)/\left(R/v_0\right)$ $= \left(2\rho_{water}/9\rho_{air}\right) Re_R \left(r_{fog}/R\right)^2$ which captures the ratio of the response time of a particle to that of the surrounding flow.[19] Here ρ_{water} and ρ_{air} are the densities of the droplet and air, respectively, μ_{air} is the viscosity of air and $\mathrm{Re}_R = \rho_{air} v_0 R/\mu_{air}$ is the Reynolds number. Large Stokes numbers ($St \gg 1$) lead to higher rates of droplet interception and a higher fog collection efficiency.

Using woven polyolefin Raschel meshes (Figure 1c, 1d), Schemenauer, Cereceda and co-workers have conducted numerous pilot-scale studies that demonstrate the feasibility of fog harvesting.[3, 5-7] A Standard Fog Collector consisting of 1m^2 of double-layered Raschel mesh is typically deployed.[6] Water collection rates ranging from 10^{-1} ℓ/m^2/day to 10^{1} ℓ/m^2/day have been reported for various locations and fog conditions.[3] Researchers have also investigated the influence of the width of the mesh fibers ($2R$), the shade coefficient (SC, *i.e.* the fractional area coverage), and the composition of the mesh material on the fog harvesting efficiency.[4, 7] Most studies have been performed in the field using uncontrolled natural fog conditions, and systematic studies of mesh-based fog harvesters under laboratory conditions have been rare.[3-8, 20, 21] Most work to date has focused on the mesh topology; the role of mesh surface wettability in fog harvesting has received little attention.[14, 20-22]

In this study, we integrate a recent theoretical analysis[4] of the hydrodynamics near a woven mesh with physico-chemical constraints that address i) the issues of clogging of the mesh by coalesced droplets and ii) re-entrainment of collected droplets in the wind. We distill the resulting composite understanding of liquid drop impact on a fiber network structure into a design chart that predicts the overall collection efficiency for a given mesh geometry in a given

fog environment. We also report experimental collection efficiencies for a homologous series of woven meshes with controlled surface chemistry that significantly exceed the current collection efficiency of the Raschel mesh under controlled laboratory conditions.

Materials and Methods

Preparation of Meshes

Raschel mesh samples with 35% shade coefficient were procured from Fogquest volunteers in Chile and were cut into 30 mm by 30 mm pieces. To keep the Raschel mesh flat and to ensure that the meshes are normal to the direction of fog stream, the three edges of square planar mesh were supported by a metal wire frame with diameter of 127 μm . Sample wire mesh surfaces were prepared by cutting commercially available wire meshes (McMaster-Carr, Corrosion-Resistant Type 304 Stainless Steel Woven Wire Cloth) into the same square planar shape with 30 mm side.

Polyolefin emulant coating (denoted by PO)

When comparing the performance of the Raschel and wire meshes, it is important to note that both the surface chemistry and the physical geometry are different. To enable us to investigate the effect of each variable independently it is thus desirable to develop a coating for the mesh that can emulate the properties of a polyolefin surface. We have previously shown that by tuning the relative concentration of the FluoroPOSS species and a compatible polymer binder (*e.g.* PEMA) we can tune the wettability characteristics of a dip-coated surface over a wide range.[23] In order to generate a coated wire mesh that closely mimics the surface properties of the

polyolefin Raschel mesh, the as-received wire mesh was dip-coated using a 1.7 wt.% 1H,1H,2H,2H-heptadecafluorodecyl polyhedral oligomeric silsesquioxane (fluorodecyl POSS) 98.3 wt.% poly(ethyl methacrylate) (PEMA, M_W = 515 kDa, Sigma Aldrich) solution in a volatile hydrochlorofluorocarbon solvent (Asahiklin AK-225, Asahi Glass Company) at a concentration of 10 mg/mℓ. The meshes were dipped for 5 minutes, and then air-dried to evaporate the solvent. Uniformity of the coating was checked by scanning electron microscope (SEM) and by contact angle measurements at multiple locations on the surface.

POSS-PEMA dipcoating (denoted by PPD)

Mesh samples were dip-coated using a 50 wt.% fluorodecyl POSS / 50 wt.% PEMA solution in Asahiklin at a concentration of 10 mg/mℓ. The meshes were dipped for 5 minutes, and then air-dried to evaporate the solvent, resulting in a smooth hydrophobic coating.

POSS-PEMA spraycoating (denoted by PPS)

A 50 wt.% fluorodecyl POSS 50 wt.% PEMA solution was prepared in Asahiklin at a concentration of 50 mg/mℓ. The superhydrophobic spray-coated meshes were prepared by spray deposition of the polymer solution using an air spray-brush (McMaster-Carr) using a pressurized nitrogen stream to produce a re-entrant microtexture with very low contact angle hysteresis.[24] A representative micrograph of the spray-coated mesh is shown in Figure S3.

Liquid Impregnated surfaces (denoted by KO)

The spray-coated meshes were immersed into nonvolatile Krytox oil (γ_{LV} = 17 mN/m at 25°C, $\mu \simeq 113$ mPa·s at 20°C, DuPont) using a DCAT 11 (DataPhysics Instruments) tensiometer at a rate of 0.5 mm/min and then retracted at the same speed. A thin film of fluorinated Krytox oil

remains imbibed into the porous spraycoated texture after the mesh is completely withdrawn from the oil bath, resulting in a "SLIPS" surface with very low contact angle hysteresis.[25-27]

Experimental Procedure

All fog collection experiments were performed at a relative humidity of RH = 100% and temperature of 26.4 ± 0.5°C in a controlled-humidity glove box (environmental chamber, Electro-Tech Systems, Inc.) to eliminate complications resulting from evaporation and condensation. Each sample was positioned 10 mm in front of the end of two plastic concentric cylinders with different diameters of 100 mm and 30 mm, respectively. As shown in Figure S5, fog droplets ($r_{fog} = 3\,\mu$m) created from a nebulizer (Omron Compair XLT Nebulizer Compressor Kit NE-C25, $\dot{Q}$=16 mℓ/hr) were convected towards the mesh sample by a wind stream of velocity $v_0 \simeq$ 2m/s, generated by a speed-tunable fan (Thermaltake Mobile Fan II External USB Cooling Fan). The concentric axis of the two cylinders and axes of symmetry of meshes and container were aligned to be on the same vertical plane. The mass of water collected in the container with dimension of 50 mm by 50 mm that was located 50 mm under the mesh samples was measured every hour for Raschel meshes and every 30 minutes for wire woven meshes to quantify the time evolution of the collection efficiency. Once the efficiency reached a steady asymptotic value, the readings from at least three consecutive experiments were averaged to calculate the fog collection efficiency.

Theoretical Basis

We introduce two dimensionless geometric groups to facilitate the mechanistic analysis of fog harvesting behavior: i) the ratio of the radius of fog droplets (r_{fog}) to the radius of the mesh wire (R); denoted by $R^* = r_{fog}/R$ and ii) a spacing ratio denoted by $D^* = (R+D)/R$ (see Figure 1e, 2a, 2b), which measures the relative openness of the weave. The more commonly reported shade coefficient (*SC*), which is the fraction of projected area that is occluded by the solid mesh fibers, can also be evaluated in terms of D^* as $SC = 2\left[1 - 1/(2D^*)\right]/D^*$. We use the design space (Figure 2c) constructed from these two parameters to identify various meshes and evaluate their fog collection efficiencies $\eta(R^*, D^*)$ using droplet impact models proposed by Langmuir and Blodgett,[19] and more recently by Rivera.[4]

As shown in Figure 1e, 2a and 2b, when fog droplets convected with a uniform velocity v_0 approach the vertical mesh surface, some of the droplets collide with the mesh fibers and are subsequently deposited, whereas others pass through the void spaces between the wires. Repeated collisions lead to continued deposition, followed by droplet coalescence and growth. When the volume of a pinned water droplet reaches a critical value sufficient for the gravitational force to overcome the integrated line forces at the liquid-solid interface, the water droplet flows down along the mesh and is ultimately collected in a container. The void spaces do not collect any droplets, but they decrease the overall wind resistance and therefore help to maintain a high droplet flux towards the mesh.

The overall collection efficiency is a product of i) the aerodynamic collection efficiency (η_a) and ii) the subsequent deposition efficiency (η_d).[4] Rivera argued that the aerodynamic collection

efficiency accounts for the fraction of fog flow that is directed towards the solid portion of the mesh. The high Reynolds number ($Re \gg 1$) flow of moist air around the porous mesh (Figure 2a) is modeled as a linear combination of the flow around an impermeable rigid solid (*i.e.* $D^* = 1$), and an unobstructed uniform flow.[4] Due to the no slip and no penetration boundary conditions at the solid surface, the wind speed is locally reduced in the vicinity of the individual mesh elements. This momentum deficit is modeled in terms of an appropriate drag coefficient for the overall structure ($C_D \simeq 1.18$)[4] and the aerodynamic collection efficiency is ultimately expressed as $\eta_a = SC \Big/ \left(1 + \sqrt{C_0 / C_D}\right)$, where C_0 is the pressure drop coefficient for a cylindrical mesh[4] given as $C_0 = 1.44\left[1.3SC + \left(SC/(1-SC)\right)^2\right]$. The collection efficiency is not simply equal to the shade coefficient of the mesh, but changes nonmonotonically with the openness of the mesh and the aerodynamic characteristics of the flow through the mesh. As D^* increases from unity (an impermeable plate), the aerodynamic collection efficiency (η_a) increases from zero as the lateral deflection of the air stream is diminished. There is a local maximum in the aerodynamic efficiency at $D^*_{crit} \simeq 3.1$ (or equivalently, $SC \simeq 0.55$), and beyond this point most fog droplets pass through the void area between wires without being deflected, consequently η_a decreases for large values of $D^* \gg 1$.[4]

The deposition efficiency (η_d) quantifies the fraction of fog droplets that are actually deposited from the population initially headed towards the solid wires. In their seminal work, Langmuir and Blodgett used numerical calculations to develop an empirical correlation for the deposition of small particles on an infinitely long cylinder.[19] They found that the deposition efficiency could be described well by an empirical expression ($\eta_d \approx St/(St + \pi/2)$), where St is

the Stokes number. This expression monotonically increases as the dimensionless radius ratio R^* increases, *i.e.* cylinders with progressively smaller radii are more efficient collectors.

The resultant overall collection efficiency from the two contributions can therefore be expressed in terms of the shade coefficient of the mesh and the Stokes number of the droplet as

$$\eta = \eta_a\left(D^*\right)\eta_d\left(R^*\right) = \left[\frac{SC}{1+\sqrt{C_0/C_D}}\right]\left[\frac{St}{St+\pi/2}\right]. \quad [1]$$

This function is plotted in Figure 2c as a contour map in R^*, D^* parameter space, assuming a wind velocity of 2 m/s and uniform droplet size $r_{fog} \simeq 3\ \mu\text{m}$, (corresponding to $0 \le St \le 4$). The contours indicate that the collection efficiency of a conventional Raschel mesh (with coordinates corresponding to $D^* \simeq 5.1,\ R^* \simeq 0.005$, and an efficiency $\eta \simeq 4.8\%$) is much lower than that of a thinner and denser wire mesh (corresponding to $D^* \simeq 3.5,\ R^* \simeq 0.024,\ \eta \simeq 12\%$). The contour map can also be used as a design chart for selecting an optimal mesh by selecting a specified value of D^* (or *SC*) and then maximizing R^* . Our chart can be employed to estimate the maximum fog collection efficiency and evaluate the amount of collected water expected for a specific mesh surface, if the characteristic wind speed of the fog (v_0), liquid water content, total mesh area, and collection time are known.

It is clear from Figure 2c that a Raschel mesh is far from the optimal mesh design for high fog collection rates. The efficiency of a square planar mesh can be increased to about 5.5%, by optimizing the effective mesh opening D^* using multiple overlapping layers of meshes for example. However, for a given value of r_{fog} , further gains in efficiency are possible only by using meshes with smaller wire radii *R* (to achieve higher values of R^*).

Results and Discussion

The theoretical collection efficiency anticipated from this design framework for meshes can be adversely affected in actual performance due to two issues that depend on the surface wettability; i) convective loss of deposited droplets (or *re-entrainment*); as shown schematically in Figure 3a and ii) clogging of the mesh with pinned droplets that modifies the local aerodynamics (Figure 3b, S2).

Re-entrainment arises from aerodynamically-induced detachment of deposited water droplets back into the air stream before they can reach the critical volume at which gravitational drainage dominates. As the small deposited water droplets coalesce, the growing droplets are influenced by the competition between aerodynamic drag forces (F_{drag}) and surface adhesion forces ($F_{adhesion}$).[28-30] When the drag force overwhelms the adhesion force, the droplets are re-entrained in the fog flow, leading to a decrease in the fog collection efficiency (Figure 3a).

In Figure 3b we identify a second problem that occurs on a mesh when the deposited liquid volume becomes large. In the clogging region, the hysteretic wetting force pinning a droplet in the interstices of the mesh exceeds the gravitational draining force when the deposited water droplet size is less than a critical volume. The void area between mesh elements can thus become occluded by these pinned (non-draining) drops, depending on the spacing of the individual fibers that form the porous mesh structure. Such clogged parts of the mesh are impermeable and deflect the local air flow, significantly hampering the overall fog-harvesting ability of the grid. The effective void fraction of the porous mesh approaches zero (or $D^{*}_{effective} \rightarrow 1$) as the mesh becomes increasingly clogged and the aerodynamic collection then becomes zero.

To overcome these two challenges and to design fog collection mesh surfaces with high efficiency in practice, we consider the two critical water drop radii - denoted r_e and r_c in Figure 3c and 3d - that control these phenomena and how they vary with the physico-chemical surface properties of the meshes. In Figure 3c, the right-most shaded region represents the range of parameter space where the aerodynamic drag force (which grows as $F_{drag} \simeq \rho_{air} v_0^2 r_{drop}^2$) exceeds the adhesion force (which grows as $F_{adhesion} \simeq \gamma_{LV}\left(1+\cos\theta_{rec}\right) r_{drop}$). Droplet re-entrainment is expected in this region when the drag force $F_{drag} > F_{adhesion}$. A detailed force balance (see Supporting Information for derivation) on a spherical cap gives a critical droplet radius at which these two forces balance each other:

$$r_e \simeq \frac{4\pi\gamma_{LV}\sin^2\theta\left(1+\cos\theta_{rec}\right)}{\rho_{air} v_0^2 C_D\left(\theta-\sin\theta\cos\theta\right)} \qquad [2]$$

where γ_{LV} is the surface tension of water, $\theta = \left(\theta_{adv}+\theta_{rec}\right)/2$ is the mean contact angle of the droplet on the surface, and θ_{adv}, θ_{rec} are the advancing contact angle and receding contact angle, respectively, (see Supporting Information for details). A droplet with radius $r_{drop} > r_e$ is susceptible to re-entrainment. To reduce re-entrainment, the slope of the adhesion force curve, which is proportional to the work of adhesion of the liquid droplet on the surface of the mesh $\gamma_{LV}\left(1+\cos\theta_{rec}\right)$, must be increased. This can be achieved in practice by lowering the receding contact angle θ_{rec}.

As the droplets grow on the mesh, gravity has to overcome the surface pinning force in order to shed these collected droplets into the collecting gutter at the base of the mesh. We compare the magnitude of the gravitational body force $F_{grav} \simeq \rho_{water} g r_{drop}^3$ with the pinning force arising from

contact angle hysteresis $F_{CAH} \simeq \gamma_{LV}(CAH) r_{drop}$, where $CAH = \cos\theta_{rec} - \cos\theta_{adv}$ is a dimensionless scalar parameter that characterizes depinning of a liquid droplet in the interstitial gap of a woven mesh with a simple square weave. Setting $F_{grav} = F_{CAH}$ gives a second critical radius for "choking" or clogging of the mesh

$$r_c \simeq \sqrt{\frac{12\gamma_{LV}(\cos\theta_{rec} - \cos\theta_{adv})}{\pi\rho_{water} g B(3 + B^2)}} \qquad [3]$$

where the coefficient $B = (1 - \cos\theta)/\sin\theta$ (see Supporting Information for additional details). Figure 3d shows that the impact of mesh-clogging as a result of contact line pinning can be reduced (*i.e.* the minimum droplet size r_c that will freely drain off the mesh is reduced) by developing surface coatings with smaller values of the contact angle hysteresis *CAH*.

For an ideal fog-collecting surface, liquid droplets convected towards the mesh and deposited on the surface will be drained quickly by gravity into the collecting gutter without loss by re-entrainment to the airflow, thus refreshing the base mesh surface for capture of new fog droplets. Design of an improved mesh to maximize fog collection efficiency thus involves the following steps: I) minimizing r_c to avoid clogging, II) maximizing r_e to reduce re-entrainment, while also III) selecting a mesh opening near the optimal aerodynamic value of $D^* \simeq 3.1$ and IV) maximizing R^* to the extent possible.

The surface forces controlling adhesion and hysteresis depend upon the physico-chemical surface characteristics of the mesh,[31] and therefore smart engineering of suitable coatings can enable woven meshes to collect fog with improved efficiency. If we can make $r_e >> r_c$ by surface modifications, then the performance degradation associated with both of the shaded regions

shown in Figure 3c and 3d can be minimized. Such a mesh surface would have both low contact angle hysteresis ($CAH << 1$) and a low receding contact angle ($\theta_{rec} \to 0$). This material challenge can be summarized in the surface modification design space shown in Figure 3e. The two important design parameters are the contact angle hysteresis (CAH) and a scaled work of adhesion ($W_a/\gamma_{LV} = 1 + \cos\theta_{rec}$) that can be exploited to rank the wetting properties of various materials for preventing clogging and re-entrainment problems. From the expression for mesh clogging (r_c) given in eq.[3], it is clear that a coating with extremely low hysteresis ($CAH \to 0$) will lead to a small value of the critical mesh half spacing (denoted D_{crit}) above which the clogging problem does not occur.

Fog harvesting setups that were previously deployed have used a double-layered Raschel mesh made of polyolefin (denoted by the superscript PO) which we measure through contact angle goniometry to have $CAH^{(PO)} = \cos\theta_{rec}^{(PO)} - \cos\theta_{adv}^{(PO)} \simeq 0.40$ (see Table 1). By contrast, a topographically smooth surface dipcoated with a blend of 50% POSS - 50% PEMA (denoted by PPD) has one of the lowest values of contact angle hysteresis reported to date; $CAH^{(PPD)} = \cos\theta_{rec}^{(PPD)} - \cos\theta_{adv}^{(PPD)} \simeq 0.06$.[23] The critical opening size for a PPD coated mesh $D_{crit}^{(PPD)} \simeq 0.41\,\text{mm}$ is significantly smaller than the value for a polyolefin mesh (which we calculate to be $D_{crit}^{(PO)} \simeq 1.5\,\text{mm}$ using eq. [3]), and therefore finer meshes, if dipcoated with POSS-PEMA, will drain water droplets more readily and be less susceptible to clogging.

This hysteretic drainage criterion involves differences in the surface energies for dewetting; however, from eq. [2] it is clear that the absolute magnitude of the receding contact angle is also important for preventing re-entrainment and subsequent loss of deposited droplets. The adhesive work (per unit area) required to pull a droplet off the surface by aerodynamic drag scales with

$W_a = \gamma_{LV}(1+\cos\theta_{rec})$. As a result of the large values of θ_{rec} (which lead to easy drop roll-off and low adhesion forces), the POSS-PEMA spraycoating (denoted by PPS) shows a smaller value of r_e than the half spacing D of most of the woven meshes used in the fog collection experiments, which explains the low collection efficiency value we measure experimentally (because of re-entrainment of deposited water droplets back into the convected air stream). Therefore, "sticky" surfaces with low receding contact angles θ_{rec} (and high W_a) promote the adhesion of droplets on solid surfaces.

The surface properties of our POSS coating can be manipulated further by altering the deposition technique as we show in Figure 4. The contact angle hysteresis CAH can be further decreased to $CAH \simeq 0.01$ by spray-coating the mesh to create a re-entrant roughened topography using POSS-PEMA.[24] However, the receding contact angle increases to $\theta_{rec} \simeq 159^\circ$. Therefore, such spray coated meshes (denoted by PPS in Figure 4) are extremely clogging-resistant, but the higher value of the receding contact angle reduces drop adhesion which leads to greater propensity for droplet re-entrainment and a lower overall collection efficiency. A liquid impregnated textured surface or "SLIPS surface"[25-27] with low CAH and low θ_{rec} can be obtained by imbibing a nonvolatile oil (*e.g.*, Krytox oil) into the pores of the spray-coated surface.[27] This liquid-impregnated surface (denoted KO in Figure 4) initially exhibits a critical droplet drainage radius (r_c) that is similar to the POSS-PEMA dipcoating (PPD), but after a short period of operation this ultimately transitions to a value that is greater than the critical radius of the original polyolefin material (PO). The reason for the increased value of r_c for the liquid-impregnated coating is described in the supporting information.

Guided by this framework relating surface wettability and fog harvesting performance, we performed a set of parametric experiments using a family of simple woven meshes with a range of surface coatings (see Materials and Methods for details). We benchmarked our results against the canonical Raschel mesh, using an artificially generated laboratory fog. Our results are summarized in Figure 4 and Table 1. As shown in Table 1, for most coating materials (which do not approach the limit $\cos\theta_{rec} \to -1$), we find that the critical radius for re-entrainment is much bigger than the clogging radius $r_e >> r_c$, and re-entrainment does not impact the fog collection efficiency under our simulated fog conditions. For a given fog condition (*i.e.*, a fixed value of r_{fog}) the critical mesh half spacing D_{crit} with a given coating to prevent the clogging and re-entrainment problems (*i.e.*, $r_c = D_{crit} < D < r_e$) can be represented as a line through the origin with positive slope D_{crit}/r_{fog}, from the following relation

$$D^* = \left(D_{crit}/r_{fog}\right)R^* + 1 . \qquad [4]$$

Therefore the high efficiency regions to the right of these lines are inaccessible with $D < D_{\text{crit}}$ due to clogging; *i.e.* in this region of Figure 5a the mesh openings are too small ($D < r_c$) and the clogged mesh grids become impermeable to airborne fog water droplets.

We first consider the polyolefin Raschel mesh (with a large measured contact angle hysteresis $CAH = \cos\theta_{rec} - \cos\theta_{adv}$, and a critical opening size $D_{crit}^{(PO)} \simeq 1.5$ mm). Because of the clogging constraint, large portions of the design space (below the red line depicted in Figure 5a) with the highest efficiency cannot be accessed and, at best, a theoretical efficiency of 5% efficiency can be obtained. As shown in Figure 5b, the measured fog-harvesting efficiency of a Raschel mesh ($D^* \simeq 5.1$) was $\eta^{(PO)} \simeq 1.8 \pm 0.5\%$, under our simulated fog conditions.

The locus of the conventional polyolefin Raschel mesh in the design space of Fig 5a is shown by the open diamond. Because it lies above the critical clogging line (*i.e.*, $D_{Raschel} > D_{crit}^{(PO)} \simeq 1.5\,\text{mm}$) it is not prone to clogging. Additional dipcoating of the Raschel mesh with a POSS-PEMA coating to reduce propensity of the clogging problem therefore does not appreciably enhance its fog collection performance. This is confirmed by sample ◆ shown in Fig 5b ($\eta \simeq 2.0 \pm 0.5\%$). To access the regions of higher efficiency shown in Figure 5a, it is clear that meshes with higher R^* are required. We therefore explore the fog-collecting performance of a series of woven wire meshes with different radii. The locus of these points in our design space is shown by the filled symbols in Figure 5c. Surfaces that are dipcoated in POSS-PEMA (to achieve smaller values of *CAH*) have a lower critical opening size $D_{crit}^{(PPD)} \simeq 0.41\,\text{mm}$, and therefore, a significantly higher fraction of the design space is free of clogging and drainage limitations. As a result, meshes with thinner fibers (higher R^*) that were previously unusable due to clogging effects can now be employed for fog harvesting and have higher shade coefficients closer to the optimal value. These finer meshes are predicted to have much higher fog collection efficiencies ($\eta \simeq 12\%$), provided a suitable low hysteresis coating is applied.

In Figure 5b, we first explore the role of surface coating alone for a particular mesh geometry. The measured efficiency increases from $\eta \simeq 1.8\%$ (for a woven mesh that is dip-coated to achieve the same surface wettability characteristics as the polyolefin Raschel mesh) to $\eta \simeq 4.6\%$ for a POSS-PEMA dipcoated woven mesh (PPD, ●) with the same radius $R \simeq 445\ \mu\text{m}$ and the same shade coefficient $SC \simeq 0.5$ ($D^* \simeq 3.5$). However, the fog-collecting efficiency of a sprayed texture (PPS, ◑) and a liquid-impregnated surface (KO, ◐) woven mesh (again with the same value of $R \simeq 445\ \mu\text{m}$) do not perform as well as the dip-coated mesh due to the predominance of

re-entrainment and clogging effects. Interaction with water droplets impacting and sliding along the Krytox-impregnated "SLIPS surface"[25-27] results in a progressive loss of the nonvolatile impregnating liquid (see Figure S4 for details). This leads to increasing contact angle hysteresis and the mesh openings start to clog, resulting in no further increase in fog harvesting efficiency. We therefore focus our optimization studies on the dip-coated surfaces as they tend to be stable over much longer timescales.

In Figure 5c, the measured fog-collecting efficiency is plotted as the wire radius is progressively decreased, keeping the weave constant ($D^* \simeq 3.5$) with the same surface coating (dip-coated with POSS-PEMA). The theoretical fog collecting efficiency $\eta\left(R^*, D^*\right)$ given by our analysis in eq. [1] above (broken line) provides a good estimate of the observed trends. The measured efficiency increases monotonically from 4.6% to 10.2% as the fiber radius decreases from $R \simeq 445$ μm to $R \simeq 172$ μm for the first 4 meshes (denoted by symbols ●, ■, ▼, and ▲ in Figure 5a) that lie in the region of the design chart where clogging is not a limiting factor. However, the finest mesh ($R \simeq 127$ μm , ▶) is located inside the hysteresis-limited region (with mesh spacing $D < D_{\text{crit}} = r_c$ calculated from eqs. [3] and [4] for a dipcoated surface with $CAH^{(PPD)} = \cos\theta_{rec}^{(PPD)} - \cos\theta_{adv}^{(PPD)} \simeq 0.06$ and $D_{crit}^{(PPD)} \simeq 0.41$ mm). Clogging once again prohibits any further increase in the efficiency. A mesh located in the clogging-prone region of the design space still collects an appreciable amount of fog ($\eta \simeq 9.1 \pm 0.4\%$), but its efficiency could be improved still further by reducing the clogging constraint imposed by eq. [3] (*i.e.*, lowering the slope of the bounding line for D_{crit}, via even lower values of *CAH*).

The maximum fog harvesting efficiency observed in our experiments is $\eta \simeq 10.2 \pm 0.9\%$ (N=3) for a fine POSS-PEMA dipcoated mesh with close to optimal weave

($R \simeq 172$ μm , $D^* \simeq 3.5$, $CAH \simeq 0.06$, shown by the symbol ▲). In Figure 5d, we show the time evolution over many hours of the fog harvesting performance for its optimal mesh and a comparison with the Raschel mesh. The optimized wire mesh collects water at a faster rate and also reaches steady state faster than the Raschel mesh because of reduced 'liquid hold-up' on the mesh surface. Thus, by an appropriate choice of the surface texture and coating chemistry, the fog harvesting efficiency for representative fog conditions (corresponding to a velocity $v_0 = 2$ m/s and fog droplet radius $r_{fog} \simeq 3$ μm) has been enhanced approximately five-fold.

Conclusion

We have presented a design framework for integrating a systematic analysis of the flow, the mesh geometry and the mesh surface properties to predict the overall fog collection efficiency of the meshes. This analysis has been supported by laboratory experiments, employing a family of coated meshes with a directed stream of fog droplets, which demonstrate a five-fold enhancement in the fog-collecting efficiency of a conventional polyolefin mesh. A comparison of theoretical fog collection efficiency across many fog conditions (see Supporting Information) indicates that the fog harvesting efficiency for the POSS-PEMA dipcoated wire mesh ($R \simeq 172$ μm , ▲) is also more robust than the conventional Raschel mesh to changes in fog conditions ($1 \le r_{fog} \le 40$ μm, $1 \le v_0 \le 10$ m/s). As a result, fog harvesting technology based on POSS-PEMA dipcoated woven meshes may be deployable in many regions of the world where the size and velocity of fog droplets are not suitable for traditional Raschel meshes to work well. The performance of these rapidly-draining woven meshes are less susceptible to daily or

seasonal changes of wind speed and direction, or temperature. Optimally-engineered surfaces can work effectively in foggy conditions for longer periods of time, and subsequently produce much more water. An alternative approach using temperature-triggered switchable surface coatings that swell and release water droplets, respectively, has recently been described by Yang and coworkers.[32] Even in a mild fog with droplet radius of $3\ \mu m$, wind speed of 2 m/s and liquid water content of 0.1 g/m^3, the optimal dipcoated mesh surface ($R \simeq 172\ \mu m$, ▲) can collect approximately two liters of water through an area of 1 m^2 per day. Using literature values for conditions in a typical Chilean fog environment[7] and our new design framework, we can estimate the amount of water that can be collected using the optimal fog harvesting mesh. Typical Chilean fog conditions are characterized by a larger droplet size and higher wind velocity ($r_{fog} \simeq 13\ \mu m$, $v_0 \simeq 6\ m/s$, corresponding to a Stokes number close to $St \sim 10^2$) In such inertially-dominated conditions, the collection rate is predicted using eq. [1] to be as large as twelve liters of water through an area of 1 m^2 per day, assuming a liquid water content of 0.7 g/m^3. From such calculations it is clear that understanding the enabling roles of surface wettability in conjunction with the physical characteristics of the woven mesh geometry (*i.e.* fiber radius and shade coefficient) expands the accessible fog harvesting design space as well as future geographic opportunities for deploying fog harvesting technology.

FIGURES

Figure 1. Natural and artificial examples of fog harvesting surfaces. (a) Slender leaves of trees (*Pinus radiata*, Image courtesy Robert Holmes). (b) A spider web decorated with droplets of water collected from fog (Image courtesy William Lee). (c) A large area man-made fog collector deployed in the Atacama Desert of Chile (4) and (d) triangular weave of the Raschel Mesh used in the Large Fog Collector. (e) The basic mechanism of fog collection by physical impaction of droplets on the mesh, collection of larger coalesced droplets, and subsequent drainage.

Figure 2. Fog flow through a woven mesh surface, and a contour plot of the fog harvesting efficiency. (a) Illustration indicating the stream surfaces of fog laden wind and their deflection after passing through a woven mesh surface. (b) An enlarged picture focusing on the interaction between incoming fog droplets and a horizontal mesh element. Droplets that are closer to the central axis are trapped on the cylindrical wire, whereas droplets closer to the periphery follow the streamline around the wire. Droplets on the wire coalesce, and once they grow past a threshold size, they drain under gravity. (c) A contour plot of the fog harvesting efficiency (η) as a function of the ratio of radius of the fog droplets to the radius of the wire ($R^* = r_{fog}/R$) and the spacing ratio of the woven mesh ($D^* = (R+D)/R$). The location of various mesh surfaces and corresponding predicted efficiencies are highlighted on the design chart.

Figure 3. Two factors that reduce collection efficiency, and the surface modification design space that depicts the relative resistance to re-entrainment and drainage. These factors affecting fog harvesting and reduce collection efficiency are (a) re-entrainment of collected droplets in the wind and (b) blockage of the mesh. (c) The plot identifies the range of droplet sizes where the forces of adhesion dominate the drag forces, and establishes a criterion for a threshold droplet size for re-entrainment. (d) A second constraint arises from comparing the weight of the droplet with the surface pinning force arising from contact angle hysteresis. The threshold size where gravity dominates hysteretic pinning can be decreased by minimizing $CAH = \cos\theta_{rec} - \cos\theta_{adv}$.

Figure 4. The design space constructed from two dimensionless parameters related to work of adhesion (abscissa) and contact angle hysteresis (ordinate) depicts the relative resistance to re-entrainment and drainage. Measured values for droplets of water ($V \simeq 10\ \mu\ell$) deposited on several different coatings are shown in the plot. Wetting characteristics corresponding to a higher work of adhesion and lower contact angle hysteresis are ideal for maximum fog collection efficiency.

Figure 5. Measured fog collection efficiency. The coordinates of various mesh surfaces tested in the laboratory are depicted on the design space in (a) and the measured fog-collecting efficiencies (N = 3) are plotted in (b) and (c). At any point to the right of the critical lines shown for the polyolefin and POSS-PEMA coating in Figure 5a (*i.e.* any point in the shaded region with $D < D_{crit}$), the mesh openings clog with liquid droplets and the fog harvesting efficiency deteriorates. (b) and (c) explore the role of the mesh coating and structure (*i.e.*, the individual fiber size R and the spacing D). In (c) the theoretical efficiency evaluated from eq. [1] is shown by a broken line. The measured fog collection efficiency increases monotonically as the radius of the wire mesh decreases from $R \simeq 445$ μm (●) to $R \simeq 172$ μm (▲), but decreases in the case of $R \simeq 127$ μm (▶) as we enter the drainage-limited zone on the design chart. The time evolution of the fog harvesting performance of the optimal wire mesh (▲) and the Raschel mesh is compared over many hours in (d). The optimal wire mesh (▲) collects more water and reaches a steady state faster than the Raschel mesh (◇).

TABLES

Table 1. The values of the receding contact angle, contact angle hysteresis, and critical radii r_e and r_c for each surface coating, with the laboratory fog condition used in the humidity chamber experiment ($v_0 \simeq 2$ m/s) and a representative value of $C_D = 0.7$. For this airstream velocity, all four of the coatings show $r_c \ll r_e$.

	Polyolefin (PO)	POSS-PEMA dipcoating (PPD)	POSS-PEMA spraycoating (PPS)	Liquid-impregnated coating (KO)
θ_{rec} (°)	85	117	159	$100 \rightarrow 77$
$CAH = \cos\theta_{rec} - \cos\theta_{adv}$	0.396	0.061	0.006	$0.034 \rightarrow 0.632$
r_e (mm)	29	7.9	0.041	$20 \rightarrow 29$
r_c (mm)	1.5	0.41	0.030	$0.42 \rightarrow 2$

ASSOCIATED CONTENT

Supporting Information. (1) Derivation of critical droplet radii r_e and r_c, (2) Time evolution of the performance of liquid-impregnated textured surfaces and schematic diagram of experimental setup for fog collection efficiency measurement, and (3) Comparison of theoretical fog collection efficiencies for mesh surfaces. This material is available free of charge via the Internet at http://pubs.acs.org.

AUTHOR INFORMATION

Corresponding Author

*Robert E. Cohen

77 Massachusetts Ave. 66-554, Cambridge, MA, USA 02139

Tel 617-253-3777

Email recohen@mit.edu

*Gareth H. McKinley

77 Massachusetts Ave. 3-250, Cambridge, MA, USA 02139

Tel 617-258-0754

Fax 617-258-8559

E-mail gareth@mit.edu

Present Addresses

† Shreerang S. Chhatre

Exxon Mobil Upstream Research Company, PO Box 2189 Houston TX, 77252

Author Contributions

The manuscript was written through contributions of all authors. All authors have given approval to the final version of the manuscript. ‡These authors contributed equally.

ACKNOWLEDGMENT

The research was supported by a Samsung Scholarship (K.-C.P.) and graduate fellowship from the MIT-Legatum Center for Entrepreneurship and Development (S.S.C). This work was also partially funded by the MIT MISTI-Chile program and the Xerox Foundation. We thank Prof. Michael Rubner and Hyomin Lee for the use of humidity chamber; Mr. Robert Schemenauer for providing the Raschel mesh sample; Prof. Juan de Dios Rivera, Prof. Pilar Cereceda and coworkers from PUC-Santiago, Chile for helpful discussions during the preparation of this manuscript.

REFERENCES

1. Food and Agricultural Organization for the United Nations, United Nations Convention to Combat Desertification, Mountain Partnership Secretariat, Swiss Agency for Development and Cooperation, and Centre for Development and Environment. Highlands and Drylands – Mountains, a Source of Resilience in Arid Regions, **2011**, Rome.

2. United Nations Educational Scientific and Cultural Organization The United Nations World Water Development Report 4: Managing Water under Uncertainty and Risk, **2012**, Paris.

3. Klemm, O.; Schemenauer, R. S.; Lummerich, A.; Cereceda, P.; Marzol, V.; Corell, D.; van Heerden, J.; Reinhard, D.; Gherezghiher, T.; Olivier, J.; Osses, P.; Sarsour, J.; Frost, E.; Estrela, M. J.; Valiente, J. A.; Fessehaye, G. M. Fog as a Fresh-Water Resource: Overview and Perspectives. *Ambio* **2012**, *41*, 221-234.

4. Rivera, J. D. D. Aerodynamic Collection Efficiency of Fog Water Collectors. *Atmos. Res.* **2011**, *102*, 335-342.

5. Cereceda, P.; Larrain, H.; Osses, P.; Faras, M., Egana, I. The Spatial and Temporal Variability of Fog and Its Relation to Fog Oases in the Atacama Desert, Chile. *Atmos. Res.* **2008**, *87*, 312-323.

6. Schemenauer, R. S.; Cereceda, P. A Proposed Standard Fog Collector for Use in High-Elevation Regions. *J. Appl. Meteorol.* **1994**, *33*, 1313-1322.

7. Schemenauer, R. S.; Joe, P. I. The Collection Efficiency of a Massive Fog Collector. *Atmos. Res.* **1989**, *24*, 53-69.

8. Lekouch, I.; Muselli, M.; Kabbachi, B.; Ouazzani, J.; Melnytchouk-Milimouk, I.; Beysens, D. Dew, Fog, and Rain as Supplementary Sources of Water in South-Western Morocco. *Energy* **2011**, *36*, 2257-2265.

9. Hamilton, W. J.; Seely, M. K. Fog Basking by the Namib Desert Beetle, *Onymacris unguicularis*. *Nature* **1976**, *262*, 284-285.

10. Parker, A. R.; Lawrence, C. R. Water Capture by a Desert Beetle. *Nature* **2001**, *414*, 33-34.

11. Dawson, T. E. Fog in the California Redwood Forest: Ecosystem Inputs and Use by Plants. *Oecologia* **1998**, *117*, 476-485.

12. Limm, E. B.; Simonin, K. A.; Bothman, A. G.; Dawson, T. E. Foliar Water Uptake: A Common Water Acquisition Strategy for Plants of the Redwood Forest. *Oecologia* **2009**, *161*, 449-459.

13. Vasey, M. C.; Loik, M. E.; Parker, V. T. Influence of Summer Marine Fog and Low Cloud Stratus on Water Relations of Evergreen Woody Shrubs (*Arctostaphylos*: Ericaceae) in the Chaparral of Central California. *Oecologia* **2012**, *170*, 325-337.

14. Andrews, H. G.; Eccles, E. A.; Schofield, W. C. E.; Badyal, J. P. S. Three-Dimensional Hierarchical Structures for Fog Harvesting. *Langmuir* **2011**, *27*, 3798-3802.

15. Zhai, L.; Berg, M. C.; Cebeci, F. Ç.; Kim, Y; Milwid, J. M.; Rubner, M. F.; Cohen, R. E. Patterned Superhydrophobic Surfaces: Toward a Synthetic Mimic of the Namib Desert Beetle. *Nano Lett*. **2006**, *6*, 1213-1217.

16. Roth-Nebelsick, A.; Ebner, M.; Miranda, T.; Gottschalk, V.; Voigt, D.; Gorb, S.; Stegmaier, T.; Sarsour, J.; Linke, M.; Konrad, W. Leaf Surface Structures Enable the Endemic Namib Desert Grass *Stipagrostis sabulicola* to Irrigate Itself with Fog Water. *J. R. Soc., Interface* **2012**, *9*, 1965-1974.

17. Sahni, V.; Harris, J.; Blackledge, T. A.; Dhinojwala, A. Cobweb-Weaving Spiders Produce Different Attachment Discs for Locomotion and Prey Capture. *Nat. Commun.* **2012**, DOI:10.1038/ncomms2099.

18. Zheng, Y.; Bai, H.; Huang, Z.; Tian, X.; Nie, F.-Q.; Zhao, Y.; Zhai, J.; Jiang, L. Directional Water Collection on Wetted Spider Silk. *Nature* **2010**, *463*, 640-643.

19. Langmuir, I.; Blodgett, K. B. A Mathematical Investigation of Water Droplet Trajectories. Collected works of Irving Langmuir **2004** (Pergamon Press, Oxford).

20. Garrod, R. P.; Harris, L. G.; Schofield, W. C. E.; McGettrick, J.; Ward, L. J.; Teare, D. O. H.; Badyal, J. P. S. Mimicking a Stenocara Beetle's Back for Microcondensation using Plasmachemical Patterned Superhydrophobic-Superhydrophilic Surfaces. *Langmuir* **2007**, *23*, 689-693.

21. Yu, T. S.; Park, J.; Lim, H.; Breuer, K. S. Fog Deposition and Accumulation on Smooth and Textured Hydrophobic Surfaces. *Langmuir* **2012**, *28*, 12771-12778.

22. Dorrer, C.; Rühe, J. Mimicking the Stenocara Beetle - Dewetting of Drops from a Patterned Superhydrophobic Surface. *Langmuir* **2008**, *24*, 6154-6158.

23. Meuler, A. J.; Chhatre, S. S.; Nieves, A. R.; Mabry, J. M.; Cohen, R. E.; McKinley, G. H. Examination of Wettability and Surface Energy in Fluorodecyl POSS/Polymer Blends. *Soft Matter* **2011**, *7*, 10122-10134.

24. Srinivasan, S.; Chhatre, S. S.; Mabry, J. M.; Cohen, R. E.; McKinley, G. H. Solution Spraying of Poly(methyl methacrylate) Blends to Fabricate Microtextured, Superoleophobic Surfaces. *Polymer* **2011**, *52*, 3209-3218.

25. Quéré, D. Non-Sticking Drops. *Rep. Prog. Phys.* **2005**, *68*, 2495-2532.

26. Wong, T.-S.; Kang, S. H.; Tang, S. K. Y.; Smythe, E. J.; Hatton, B. D.; Grinthal, A.; Aizenberg, J. Bioinspired Self-Repairing Slippery Surfaces with Pressure-Stable Omniphobicity. *Nature* **2011**, *477*, 443-447.

27. Smith, J. D.; Dhiman, R.; Anand, S.; Reza-Garduno, E.; Cohen, R. E.; McKinley, G. H.; Varanasi, K. K. Droplet Mobility on Lubricant-Impregnated Surfaces. *Soft Matter* **2013**, *9*, 1772-1780.

28. Paxson, A. T.; Varanasi, K. K. Self-Similarity of Contact Line Depinning from Textured Surfaces. *Nat. Commun.* **2013**, DOI:10.1038/ncomms2482.

29. Milne, A. J. B.; Amirfazli, A. Drop Shedding by Shear Flow for Hydrophilic to Superhydrophobic Surfaces. *Langmuir* **2009**, *25*, 14155-14164.

30. Ledesma-Aguilar, R.; Nistal, R.; Hernández-Machado, A.; Pagonabarraga, I. Controlled Drop Emission by Wetting Properties in Driven Liquid Filaments. *Nat. Mater.* **2011**, *10*, 367-371.

31. Quéré, D. Wetting and Roughness. *Annu. Rev. Mater. Res.* **2008**, *38*, 71-99.

32. Yang, H.; Zhu, H.; Hendrix, M. M. R. M.; Lousberg, N. J. H. G. M.; de With, G.; Esteves, A. C. C.; Xin, J. H. Temperature-Triggered Collection and Release of Water from Fogs by a Sponge-Like Cotton Fabric. *Adv. Mater.* **2013**, *25*, 1150-1154.

Table of Contents Only

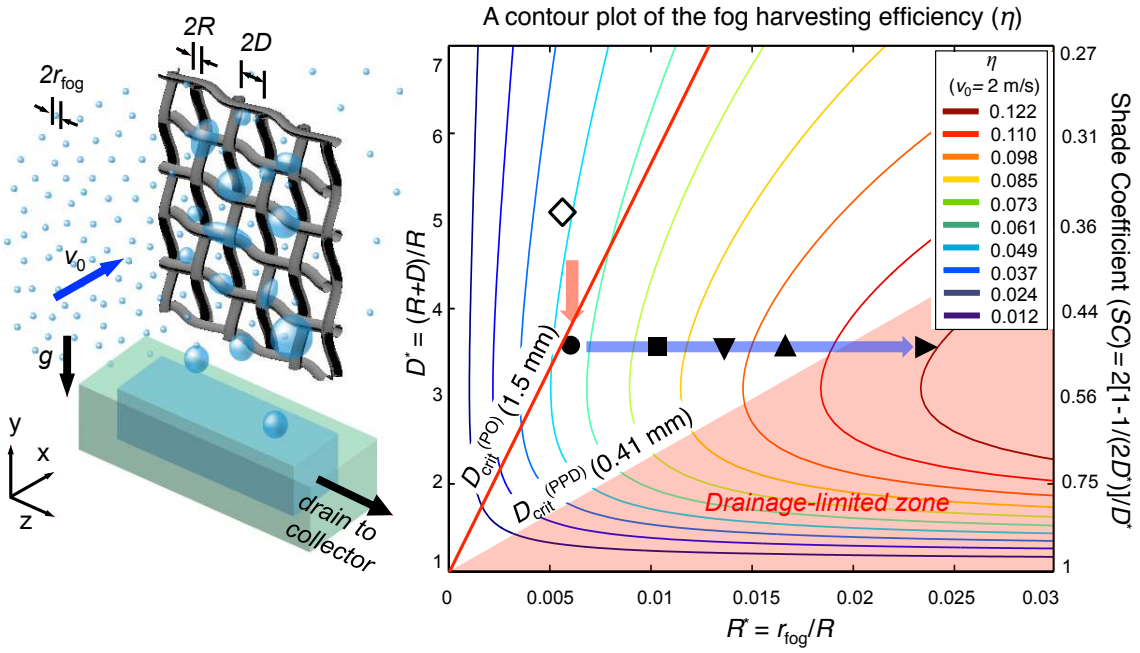

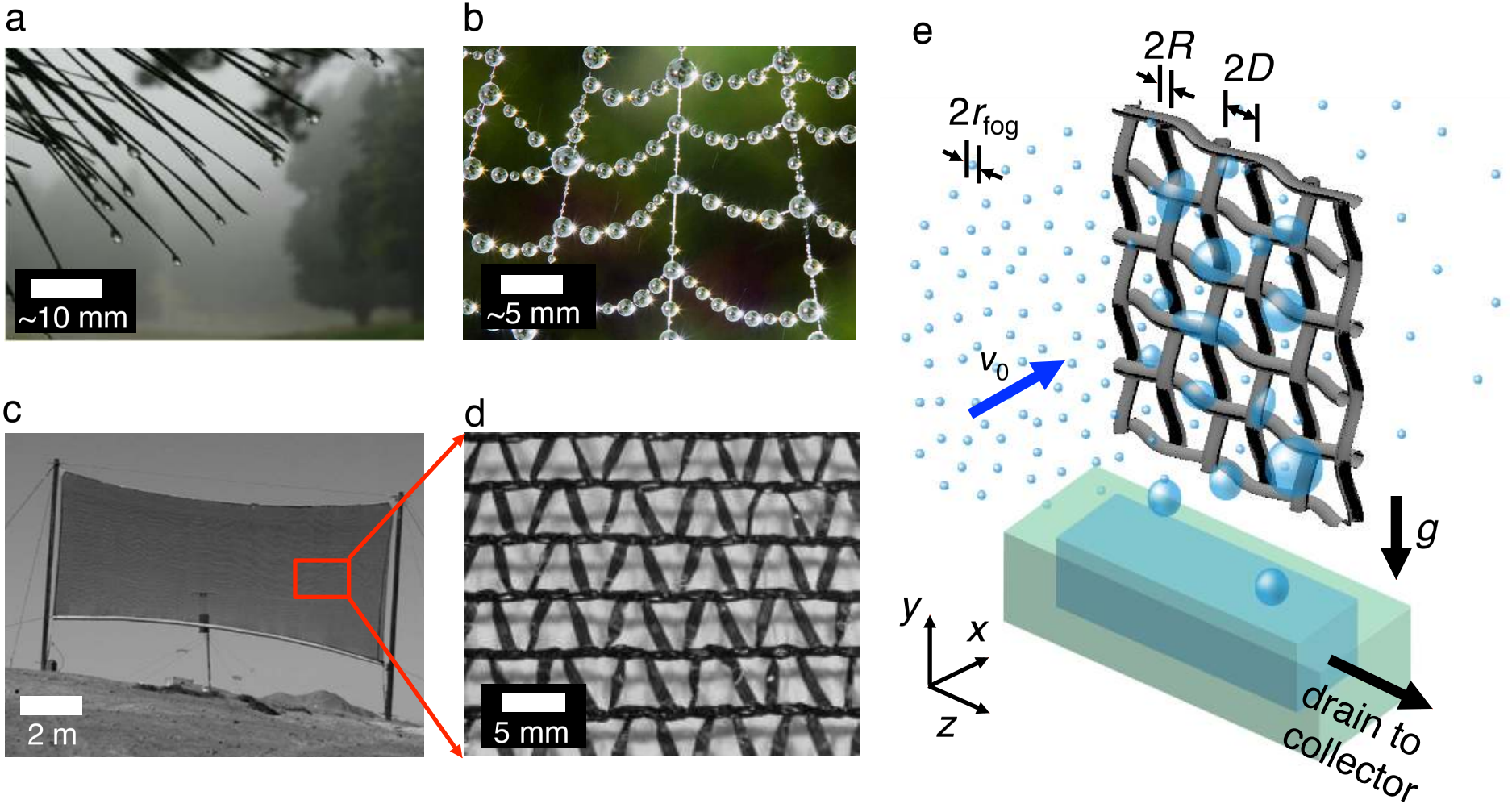
a
~10 mm
b
~5 mm
c
2 m
d
5 mm
e
2R
2D
2r_fog
v_0
g
y
x
z
drain to collector

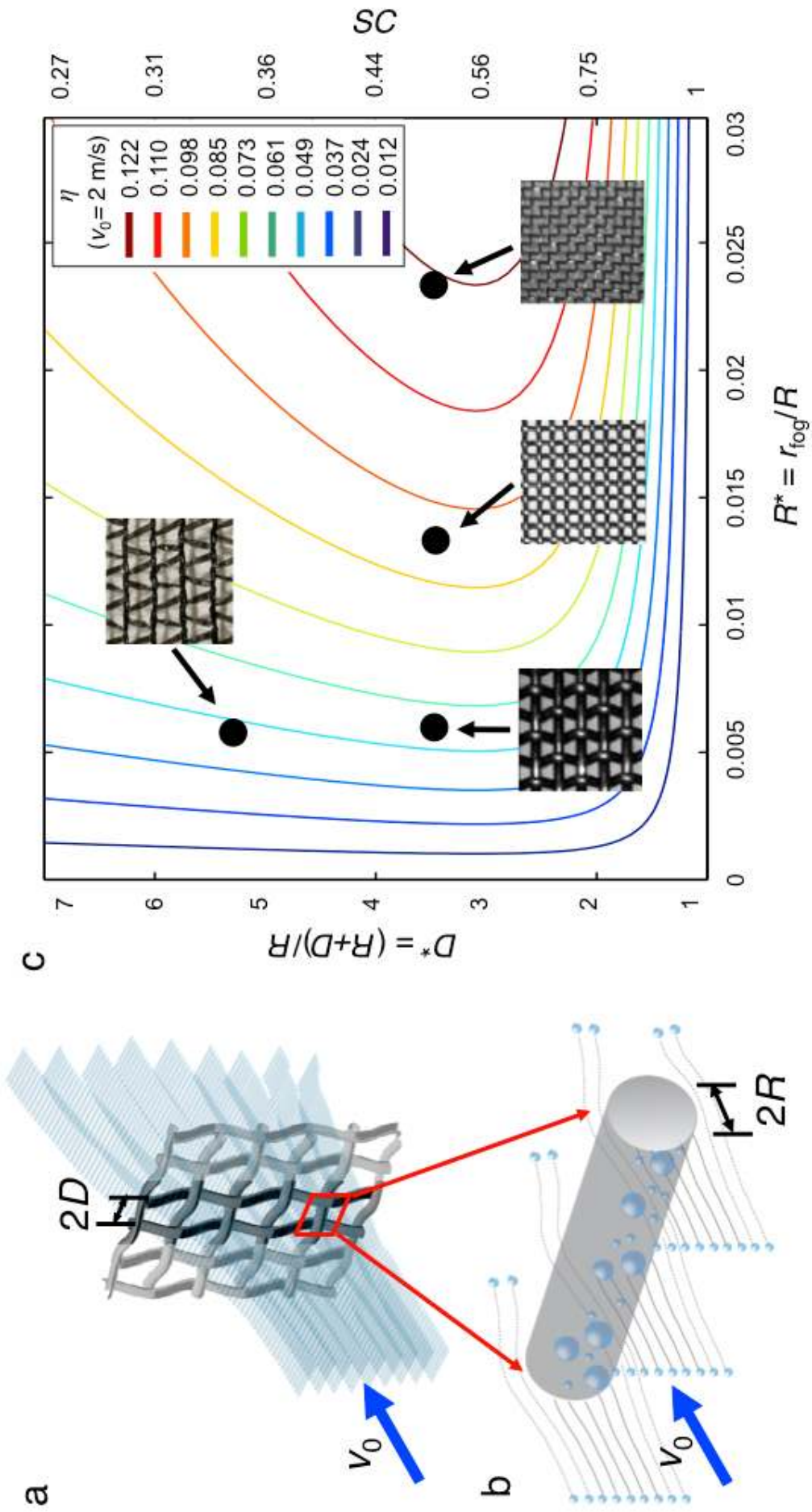
SC
0.27
0.31
0.36
0.44
0.56
0.75
1
η
(v_0= 2 m/s)
0.122
0.110
0.098
0.085
0.073
0.061
0.049
0.037
0.024
0.012
$R^* = r_{fog}/R$
0
0.005
0.01
0.015
0.02
0.025
0.03
$D^* = (R+D)/R$
7
6
5
4
3
2
1
c
2D
2R
v_0
v_0
a
b

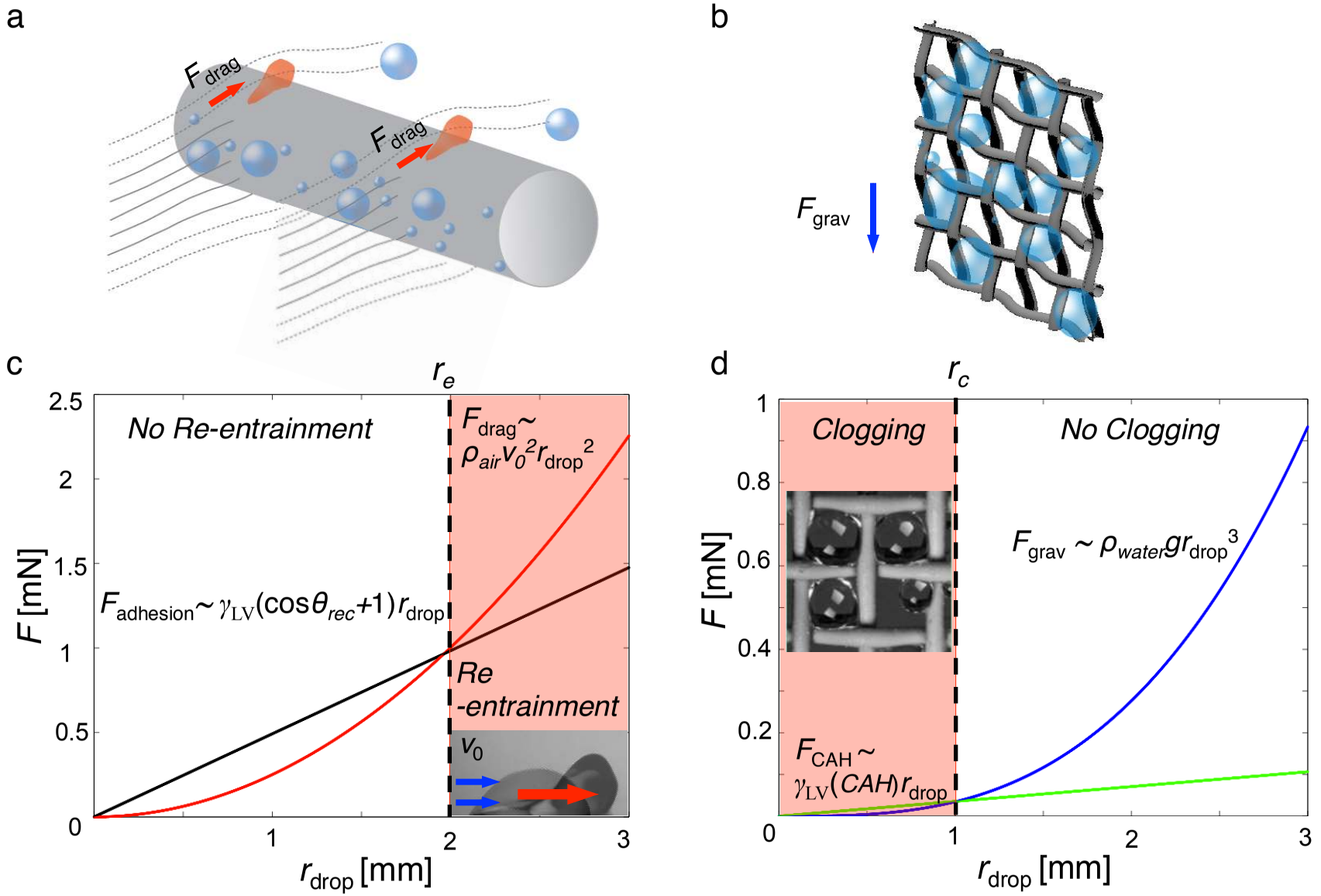
a
F_{drag}
F_{drag}
b
F_{grav}
c
r_e
No Re-entrainment
F_{drag}~ $\rho_{air} v_0^2 r_{drop}^2$
$F_{adhesion}$~ $\gamma_{LV}(\cos\theta_{rec}+1) r_{drop}$
Re -entrainment
v_0
F [mN]
r_{drop} [mm]
d
r_c
Clogging
No Clogging
F_{grav} ~ $\rho_{water} g r_{drop}^3$
F_{CAH} ~ $\gamma_{LV}(CAH) r_{drop}$
F [mN]
r_{drop} [mm]

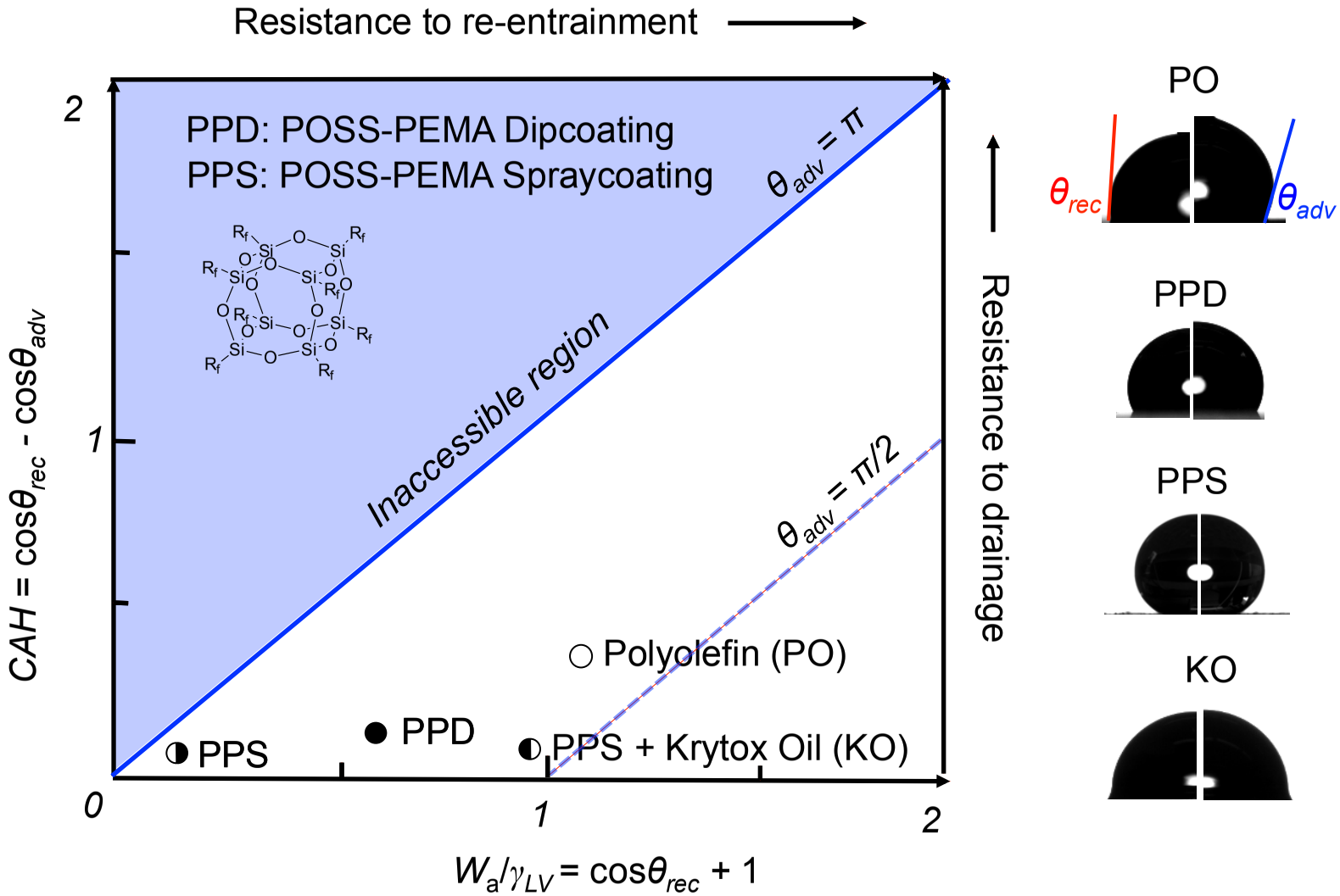
Resistance to re-entrainment
PPD: POSS-PEMA Dipcoating
PPS: POSS-PEMA Spraycoating
θ adv = π
Inaccessible region
θ adv = π/2
Polyolefin (PO)
PPS
PPD
PPS + Krytox Oil (KO)
Resistance to drainage
CAH = cosθrec - cosθadv
Wa/γLV = cosθrec + 1
0
1
2
PO
θrec
θadv
PPD
PPS
KO

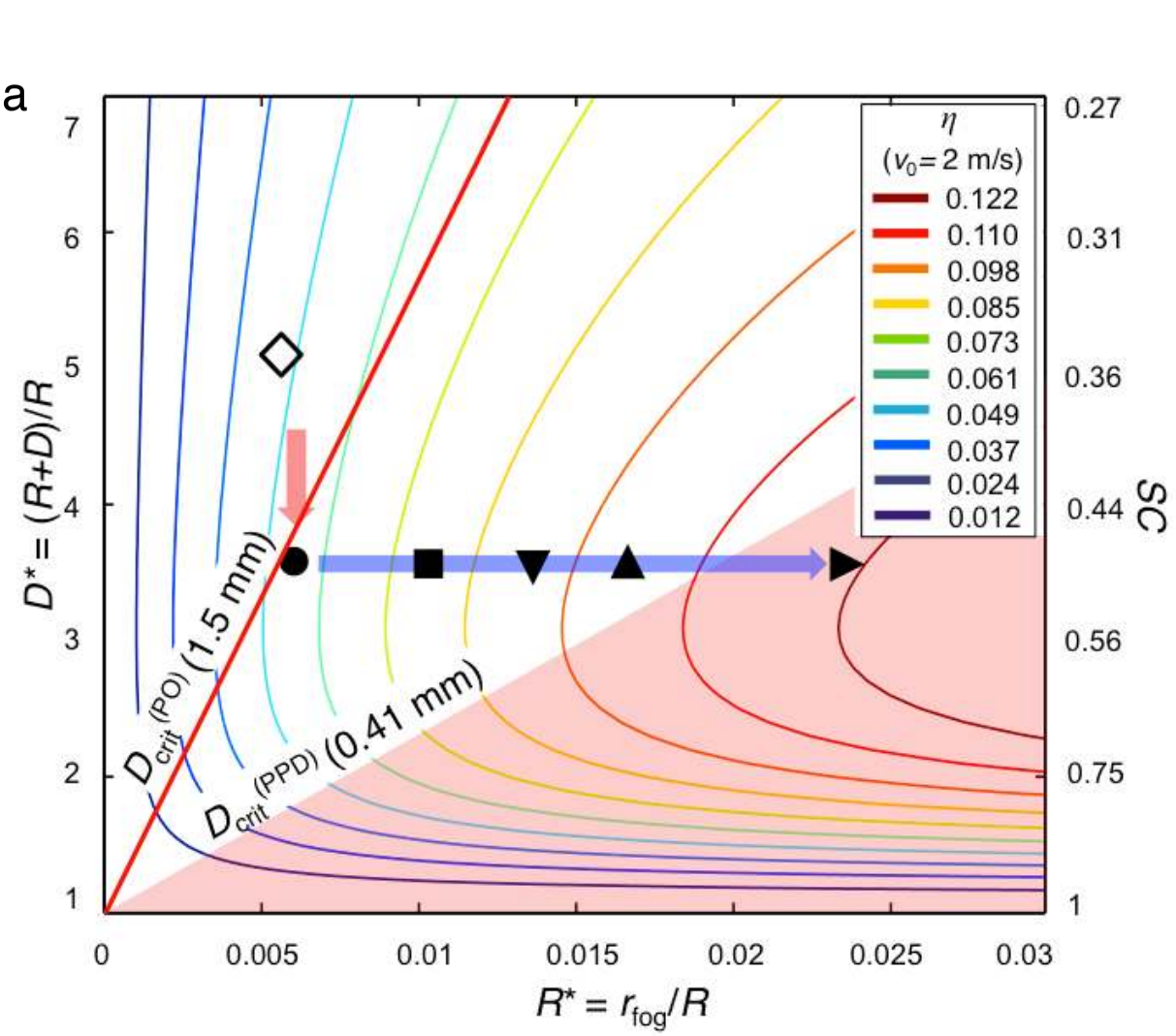
a
$D^* = (R+D)/R$
$R^* = r_{fog}/R$
SC
η (v_0 = 2 m/s)
0.122
0.110
0.098
0.085
0.073
0.061
0.049
0.037
0.024
0.012
$D_{crit}^{(PO)}$ (1.5 mm)
$D_{crit}^{(PPD)}$ (0.41 mm)

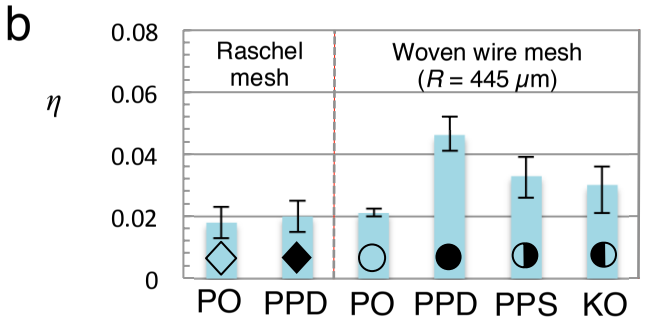
b
η
Raschel mesh
Woven wire mesh (R = 445 μm)
PO
PPD
PO
PPD
PPS
KO

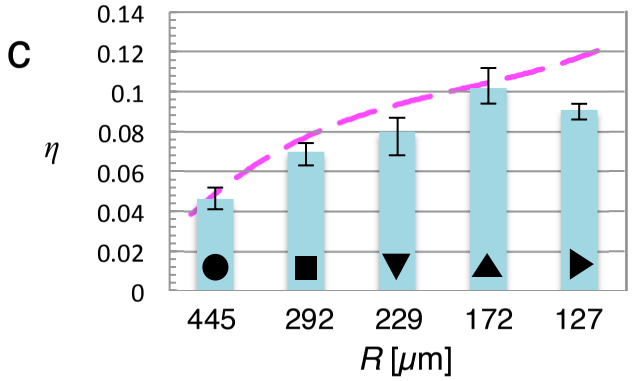
c
η
445
292
229
172
127
R [μm]

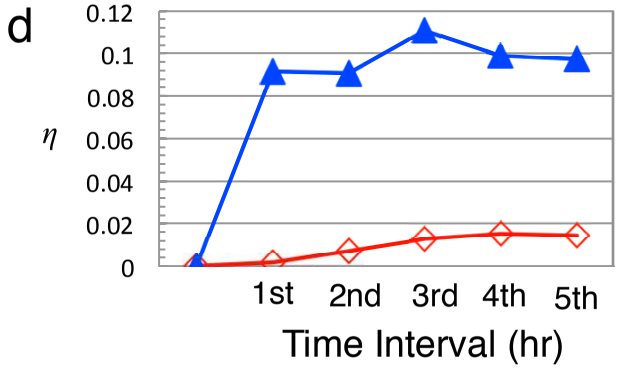
d
η
1st
2nd
3rd
4th
5th
Time Interval (hr)